NF-κB Epigenetic Attractor Landscape Drives Breast Cancer Heterogeneity

Francisco Lopes[1,2]*, Bruno R. B. Pires[3,4], Alexandre A. B. Lima[1], Renata Binato[4], Eliana Abdelhay[4]

[1]Developmental Biology and Dynamical Systems Group, Universidade Federal do Rio de Janeiro, Campus Duque de Caxias Professor Geraldo Cidade; Duque de Caxias, Brazil.

[2]Institute for Quantitative and Computational Biosciences, University of California Los Angeles; Los Angeles, USA.

[3] Department of Biophysics and Biometrics, Universidade Estadual do Rio de Janeiro; Rio de Janeiro, Brazil.

[4]Stem Cell Laboratory, Divisão de Laboratórios Especializados, Instituto Nacional de Câncer; Rio de Janeiro, Brazil.

*Corresponding author: flopes@ufrj.br

Development of subtype heterogeneity in breast cancer requires stochastic transitions between cell types. Here, we sought to characterize how NF-κB contributes to breast cancer progression. We built a gene regulatory network model and calibrated it to the expression levels of NF-κB, TWIST1, SIP1, and SLUG in HER2+ and TNBC cell line, using patient and *in vitro* published data for validation. The model's epigenetic landscape exhibits two attractor basins separated by a fluctuation-susceptible slow route. NF-κB stochastic fluctuations induce irreversible transitions from HER2+ to TNBC basins at different times, increasing heterogeneity. Mutations altering the availability of NF-κB change the size of the subtype basins, changing the transition probabilities. Our findings enhance the established attractor landscape formulation and deepen understanding of breast cancer heterogeneity.

INTRODUCTION

To understand how cell differentiation occurs rapidly during embryonic development, Waddington proposed his famous metaphor, comparing the sequential events of cell differentiation to a ball rolling down a bifurcated valley (*1*), Fig. 1A. Later, using the dynamic systems theory, Kauffman (*2*) proposed the concept of cell types as attractors. According to this concept, all cell types correspond to different attractors in a multidimensional space, with biochemical fluctuations inducing transitions between these stable states. Building on this foundation, Wang and collaborators have recently proposed a systematic approach to determine and characterize Waddington's epigenetic landscape, making it no more a metaphor (*3*). Despite these advances, some critical questions still need to be addressed. For instance, cell differentiation is more common than dedifferentiation, suggesting that transitions between attractor states exhibit a preferential direction from undifferentiated to differentiated cell states.

Breast cancer (BC) is commonly classified into three subtypes: luminal, characterized by high expression of estrogen receptors (ER) and often progesterone receptors (PR); HER2-positive (HER2+), marked by overexpression of the epidermal growth factor receptor 2 (HER2); and triple-negative breast cancer (TNBC), which lacks expression of ER, PR, and HER2 (*4*). Using single-cell RNAseq (scRNAseq) to classify cells from the same BC patient sample, Chung and collaborators (*5*) found remarkable heterogeneity (Fig. 1B). Wu et al. (*6*) also revealed significant heterogeneity in samples from luminal, $HER2^+$ and basal (TNBC) patients using scRNAseq data.

The NF-κB family consists of five subunits (RelA/p65, NF-κB1/p50, NF-κB2/p52, c-Rel, and RelB) that form various homo- and heterodimers, with p65/p50 being the most prevalent (*7*). In resting cells, NF-κB is bound and inhibited by IκB complexes, consisting of IκBα, IκBβ, and IκBε subunits. The activation of NF-κB signaling has been associated with numerous pathological conditions, including chronic inflammation (*8*), heart (*9*) and immune (*10*) diseases, and various types of cancer (*11–16*). In cancer cells, NF-κB signaling is involved in diverse mechanisms like cancer initiation, uncontrolled proliferation, metastasis, and therapy resistance (*16*). We have previously shown that, at the transcriptional level, NF-κB directly activates EMT transcription factors (EMT-TFs) SNAI2/SLUG, ZEB2/SIP1, and TWIST1, playing a critical role in the regulation of EMT-TFs, which is a characteristic of $HER2^+$ and TNBC cells (*17*). Our results here support the epigenetic attractor landscape general model. The Gene Regulation Network (GRN) exhibits two attractor basins corresponding to the HER2+ and TNBC subtypes, separated by an unstable stationary state. Stochastic fluctuations in the NF-κB levels induce a spontaneous irreversible transition from HER2+ to TNBC attractor basins at different times, contributing to subtype heterogeneity. The unstable state mediates the transition by providing a slow, dynamic-fluctuations susceptible route between both subtypes in the phase space. Mutations that change the availability of NF-κB alter the size of the subtype basins, changing the transition probabilities. Our findings highlight the need to develop therapies that prevent or slow these stochastic transitions between states.

RESULTS

The GRN reproduces NF-κB dynamics in HER2$^+$ and TNBC cells

To describe the molecular mechanism responsible for the role of NF-κB for BC progression, we performed RT-qPCR assays characterizing NF-κB relative expression levels and its EMT-related target genes, TWIST1, SNAIL, SLUG in two well-described BC cell lines of HER2$^+$ and TNBC subtypes, HCC-1954 and MDA-MB-231, respectively (**Fig. 1C**). We then built a GRN model assuming gene interactions already described in the literature (**Fig. 1D**). In this model, the NF-κB heterodimer (p65:p50) activates the expression of TWIST1, SNAIL, SLUG (*17*) and both subunits p50 and p65 (*18*, *19*). The chemical reaction network theory (*20*, *21*) indicates that the model can exhibit two stable stationary states.

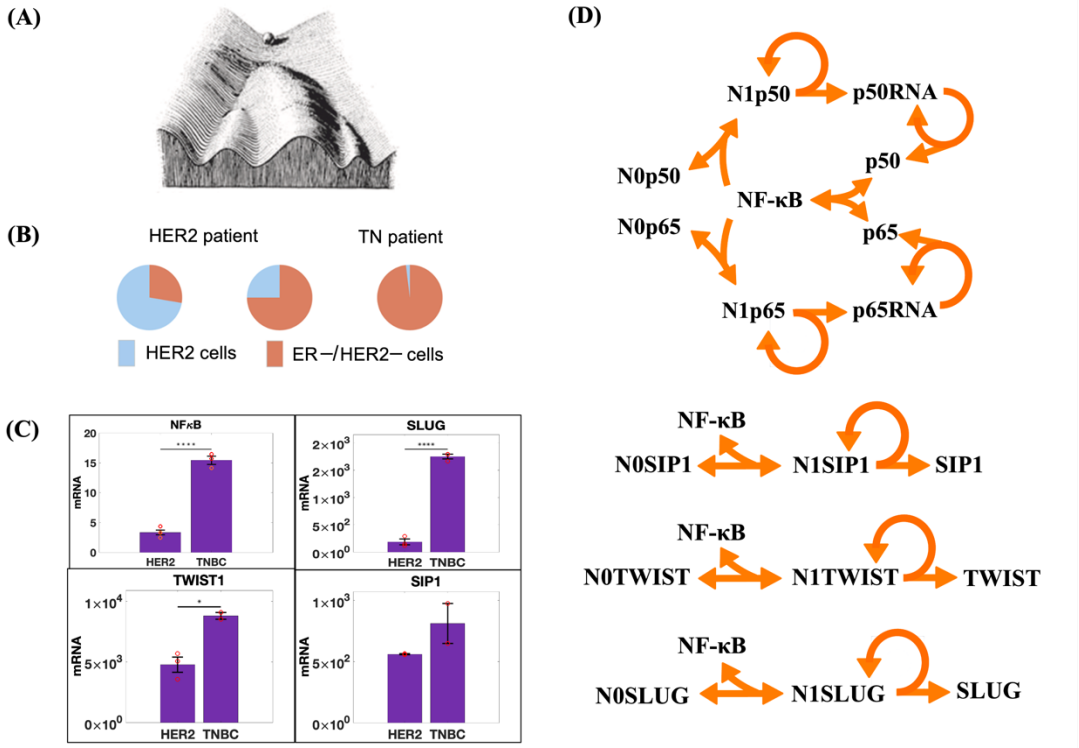

Fig. 1. Model for the activation of SLUG, SIP1, TWIST1, and NF-κB (subunits p50 and p65). (A) Waddington epigenetic landscape metaphor. **(B)** BC heterogeneity determined by scRNAseq (5): proportion of HER2 and ER-/HER2- cells in two HER2 and one TNBC classified patient. **(C)** Quantitative PCR (qPCR) analysis of NF-κB, TWIST1, SLUG, and SIP1 expression levels in HCC-1954 (HER2$^+$) and MDA-MB-231 (TNBC) cell lines, ****, ***and * indicates $p < 0.0001$, $p < 0.001$ e^{-3} and $p < 0.2$ statistical significance, respectively. RNA levels were estimated from our TR-qPCR data compared to the estimated number of RNA molecules in a mammalian cell (Table S1). Purple bars: Calibration of the GRN model depicting transcriptional regulation of SLUG, SIP1, TWIST1 and NF-κB subunits (p50 and p65) by the p50-p65 NF-κB dimer. **(D)** Representation of model reactions: N0X or N1X indicates whether the regulatory region of gene X is empty or occupied by a NF-κB dimer. Gene activation is described by a three-step reaction: a reversible reaction for NF-κB binding (NFκB + N0X ↔ N1X), and two irreversible reactions for mRNA (N1X → XRNA) and protein synthesis (XRNA → X). Constitutive synthesis and degradation of RNAs, and protein degradation are also assumed. Detailed reactions on Fig. S1.

After model calibration (Fig. 2A), we decided to verify the model's capacity to reproduce the dynamic behavior of these genes by determining the recovery time of their expression levels in both HER2$^+$ and TNBC subtypes after cell treatment with the NF-κB inhibition Dehydroxymethylepoxyquinomicin (DHMEQ) (Fig. 2B). We fine-tuned the model parameters to reproduce this RNA recovery without affecting the Fig. 2A calibration. The model successfully reproduced recovery times similar to those observed in both cell lines (Fig. 2B). The only exception is SLUG, where experimental recovery times differ between HER2$^+$ and TNBC subtypes. This suggests that other genes might contribute to the faster SLUG recovery in TNBC. Indeed, the high SLUG at level (8 hours) in TNBC cells (purple bars) compared to HER2$^+$ cells suggests additional transcriptional regulators besides NF-κB in TNBC. Since such factors are not described in the GRN model, this effect could not be reproduced.

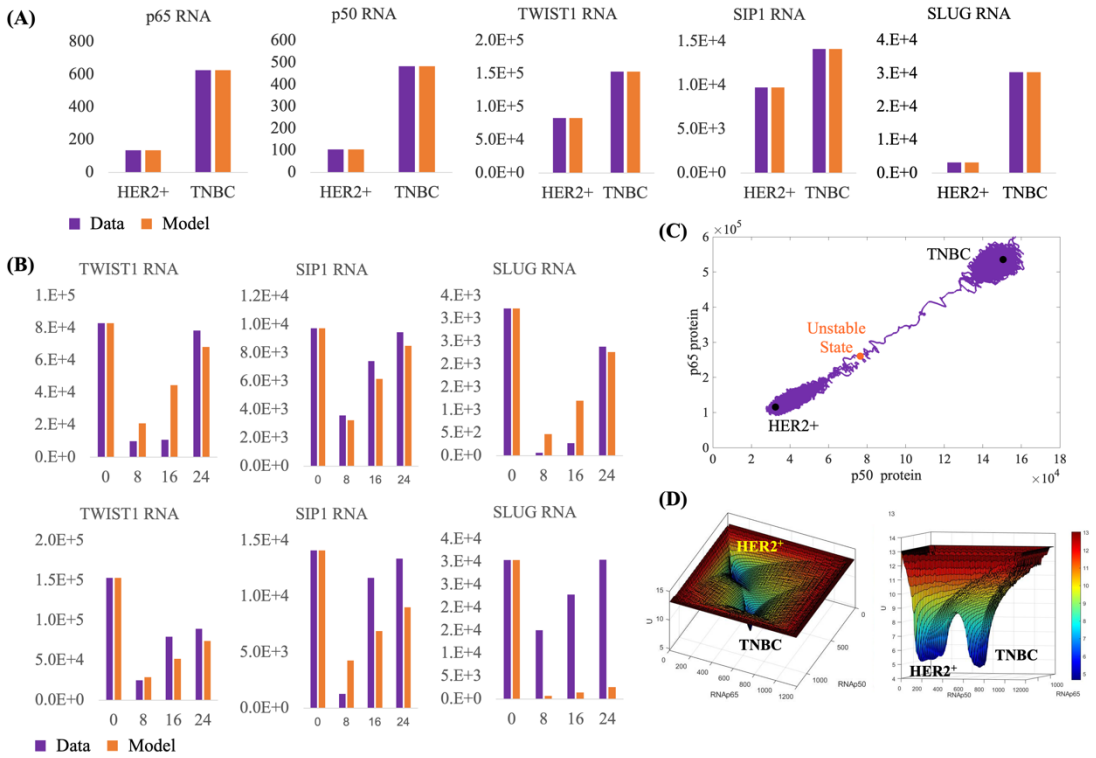

Fig. 2. The epigenetic attractor landscape exhibits one attractor associated with each BC subtypes. **(A)** Model calibration to estimated protein and RNA molecule numbers of NF-κB subunits p50, p65, and the transcription factors SLUG, SIP1 and TWIST, using data from Fig. 1C. **(B)** Model parameters fine-tuned to reproduce the temporal dynamics of expression level recovery in HER2$^+$ and TNBC cell subtypes following treatment with the NF-κB inhibitor DHMEQ. **(C)** Three stationary states and one transition trajectory in the p50 *x* p65 phase space. **(D)** Two distinct perspectives of the model attractor basins.

The GRN exhibits an attractor landscape with two basins

To describe the model phase space, we solved the algebraic equations derived from the Ordinary Differential Equations (ODEs, Fig. S2) finding three stationary states (Fig. 2C). Both

black circle states have seven eigenvectors with negative eigenvalues and two with null eigenvalues. Between these stable states, there is one unstable one. We then built the model epigenetic attractor landscape by performing 10 thousand deterministic simulations, starting at different uniformly-distributed positions in the p50 x p65 RNA phase space, Fig. 2D. This surface exhibits two basins of attraction, each containing the stationary position of one of the BC cell subtypes, and two distinct chreods both passing around the intermediate unstable position at the top of the intermediate hill (Fig. 2D). The TNBC basin is more symmetric than the HER2$^+$ one, as shown in Fig. 2C. Also, the unstable position is closer to the HER2$^+$ basins than to TNBC one. All these characteristics are discussed in depth in the following sections.

Stochastic Fluctuations induce the HER2+ to TNBC Transition

According to Kauffman's cancer attractors model (*2*, *22*), stochastic fluctuations in gene expression drive the transition between attractor states, which are associated with different cell types. To test if our modeling corroborates Kauffman's hypothesis, we plotted the trajectory of a 38-year single-cell stochastic simulation in the p50 x p65 protein phase space, Fig. 2C. The cell simulation follows a trajectory that visits different positions around the equilibrium state in the HER2$^+$ attractor (Movie S1). These positions have a strong asymmetrical distribution, resembling the shape of the HER2$^+$ basin and suggesting confinement within it (Fig. 2D). While confined to this basin, the trajectory is restricted to the region between the HER2$^+$ stable and the central unstable state; however, if the trajectory eventually passes through the position of the unstable state, it is strongly attracted towards the TNBC basin. Once there, the trajectory becomes more symmetrical than in the HER2$^+$ basin, resembling the shape of the TNBC basin. We see that the stochastic trajectory is spontaneously moving from the HER2$^+$ to the TNBC basin of attraction. This result corroborates the Kauffman's cancer attractors hypothesis showing that, at the microscopic level, stochasticity in the protein and RNA levels induces the transition between the attractor basins.

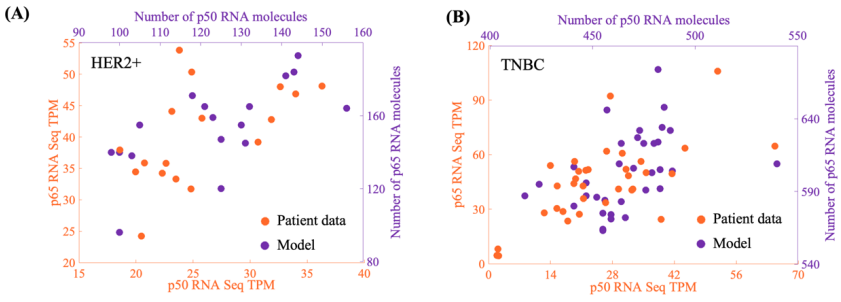

(C) **Correlations**

	Patient correlation	p value	Correlation from plotted simulation	p value	Mean correlation from 100 simulation	SD	Mean p value	SD
HER2	0.60	$1.2e^{-2}$	0.66	$3.7e^{-3}$	0.73	$5.7e^{-2}$	$1.6e^{-3}$	$1.4e^{-3}$
TNBC	0.56	$6.5e^{-4}$	0.56	$5.8e^{-4}$	0.52	$0.04.0e^{-2}$	$2.0e^{-3}$	$1.3e^{-3}$

Fig. 3. GRN validation with non-treat patient cohort data (23, 38). Orange indicates data; purple indicates model simulation **(A)** Comparison of data from 17 HER2+ patients with 17 randomly selected single-cell stochastic simulations from our set of 120 simulations. **(B)** Comparison of data from 34 TNBC patients with 34 single-cell simulations, similar to (A). **(C)** Correlation analysis of the patient data, the selected simulations, and the entire set of 120 single-cell simulations.

Given that the asymmetrical shape of the trajectory in both basins can be crucial for the correlation between positions in the phase space, we decided to compare the correlation between p50 and p65 RNA levels from our simulations with a cohort of basal and HER2$^+$ untreated Asian patients (n=51)(*23–25*). In Fig. 3A and B we show a set of simulations exhibiting a Spearman correlation (Sc) of 0.66 (p=3.7e^{-3}) for HER2$^+$ and 0.56 (p=5.8e^{-4}) for TNBC simulations. These results align with the data from untreated patients (*23*), which show Sc = 0.60 (p = 1.0e^{-2}) for HER2$^+$ and Sc = 0.56 (p = 6.5e^{-4}) for TNBC (Fig. 3A-C). They also align with Chung et al. (*5*), who found a higher cell-to-cell correlation in TNBC than in HER2$^+$.

The unstable state mediates the HER2+ to TNBC transition

To understand what drives the cell dynamics to escape from the HER2$^+$ toward the TNBC basin of attraction, we projected the only eigenvector with a positive eigenvalue, along with some other weak eigenvectors (eigenvalues ranging from 1.0e^{-3} to 1.0e^{-1}; see Fig. S3), into the 3D p50*x*p65*x*NF-κB phase space, (Fig. 4A, upper panel). These weak eigenvectors are more susceptible to being overcome by stochastic fluctuations. This susceptibility is key to understanding the transition trajectory depicted in Fig. 2C.

Initially, the trajectory is restricted to the HER2$^+$ attractor, where it started (Fig. 4A). It then fluctuates along the green eigenvector (weak, eigenvalue = - 6.0e^{-3}) associated with the HER2$^+$ stationary state. The lower panel in Fig. 4A (and Movie S2) shows a 3D plot of the time course from the same simulation. The dotted blue lines indicate that while the trajectory mainly fluctuates near the HER2$^+$ stable position, it moves toward the orange (weak) eigenvector twice but falls short of reaching the unstable position (red sphere). Only on the third instance does the trajectory reach the unstable position, moving past it and into the TNBC basin of attraction.

This dynamic effectively utilizes the weak eigenvectors' susceptibility to fluctuations. Although the red eigenvector (eigenvalue = + 2.5e^{-3}) tends to drive the trajectory away from the unstable red position, the fluctuations eventually prevail. Once past the unstable point, the trajectory follows the direction of the orange eigenvector, moving away from the red circle and towards the TNBC stable position. When the trajectory shifts from the orange to the green eigenvector (eigenvalue = - 3.2e^{-3}), it continues toward the TNBC position. Once there, it fluctuates around the TNBC stable position. Notably, none of an additional set of 120 simulations over 20 years, starting in the TNBC stable position, showed a transition back to the HER2$^+$ basin.

Spontaneous transitions from HER2+ to TNBC generate tumor heterogeneity

To investigate whether microscopic stochasticity translates into macroscopic heterogeneity in cell collectives (tissues), we ran 120 identical single-cell simulations over a model period of 20 years, all starting from the HER2$^+$ subtype's central stationary state. Assuming no cell-to-cell signaling, all HER2$^+$ cells transformed into TNBC (Fig. 4B, C), transitioning randomly at different times without reverting back. This result suggests that in a tissue, stochastic fluctuations in gene expression levels can lead to remarkable epigenetic

variations among genetically identical cells. Consequently, this epigenetic variability, resulting from asynchronous HER2+ to TNBC subtype transitions, leads to the coexistence of different cell subtypes in the same tissue, which is a crucial characteristic of intratumoral heterogeneity.

To validate our results, we compared our 120 stochastic simulations with the study by Chung et al. (*5*, *24*), which involved scRNAseq of 515 cells from 10 chemotherapy-naive BC patients and revealed significant intratumoral heterogeneity. In their classification of individual cells, they reported cases such as a sample from a HER2$^+$ patient with approximately 16% or 45% of cells categorized as ER$^-$/HER2$^-$, and a TNBC patient with around 1% of cells classified as HER2$^+$ (Fig. 4D, upper panel). By compiling the number of cells that exhibited a transition from HER2$^+$ to TNBC at 1.6, 7.15, and 15 years in the model timeframe, we successfully reproduced the relative proportions of cells in each subtype as observed in their study (Fig. 4E, lower panel).

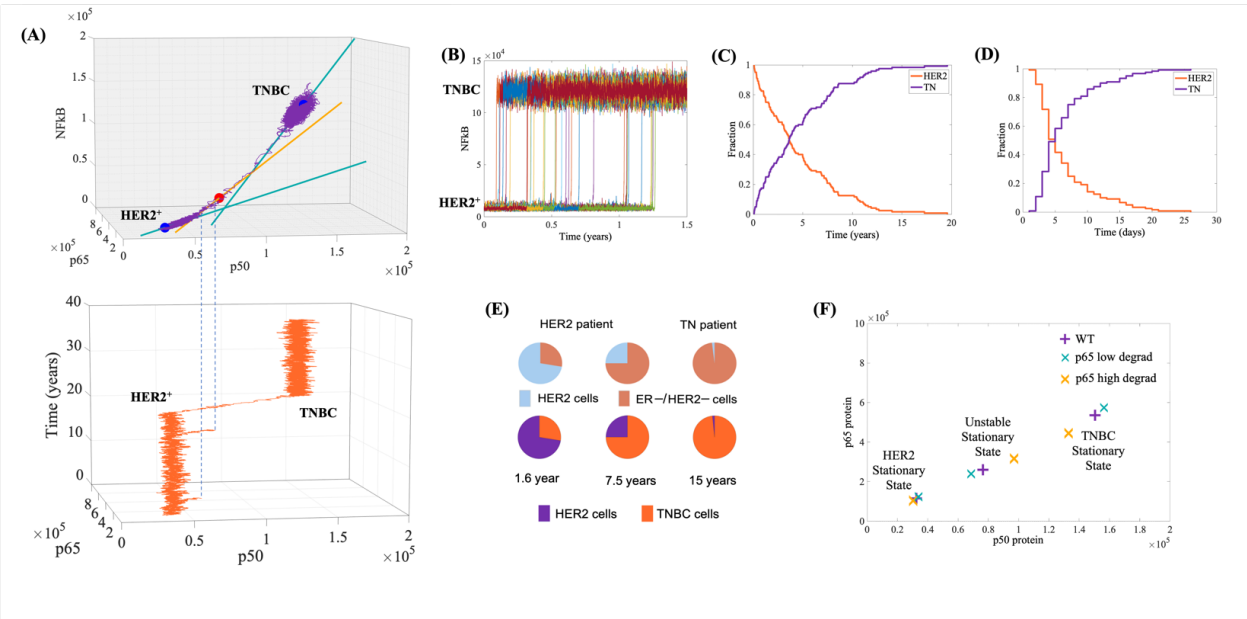

Fig. 4. The unstable state provides a route for HER2+ to TNBC subtype transition. **(A)** Upper panel: Projection of some weak eigenvectors within the p65 *x* p50 *x* NFκB phase-space. The purple line represents a single-cell simulation trajectory. Lower panel: time variation of p50 and p65 protein levels in the same simulation. **(B)** Spontaneous HER2$^+$ to TNBC transitions at different times within a period of 1.5 years collected from 120 single-cell stochastic simulations. These simulations exhibit 100% transitions over a period of 20 years, shown in **(C)**. **(D)** decreasing p65 degradation by 2.5% significantly shortens the time to reach 100% to just 26 days. **(E)** Snapshots from different time points in the 120 simulations, shown in (C), reproduce the tumor heterogeneity reported by Chung et al (5). **(F)** p50*x*p65 phase space with the model stable positions for the indicated genotype.

Mutations increase transition probabilities by changing the sizes of attractor basins

Kauffman and collaborators (*2*, *22*) have previously proposed that mutations lowering the epigenetic barrier facilitate transitions between adjacent attractors. Recently, Ren et al. (*26*) demonstrated that changing FBXW2, a protein affecting p65 degradation, alters cell proliferation and drug resistance: reducing FBXW2 increases p65 and cell growth, while increasing FBXW2 decreases p65 and inhibits growth, also affecting paclitaxel resistance. In our study, we investigate the impact of these FBXW2 mutations by simulating changes in the degradation rate

of the p65 protein. In HER2$^+$ cells, decreasing p65 degradation by 2.5% raised its levels by 6.7%, while increasing degradation by 5.0% reduced p65 levels by 10.0% (Fig. 4F, Table 1). These changes in p65 degradation altered the HER2$^+$ attractor basin size: increasing p65 degradation reduced the distance between the stable and intermediate unstable state by 19.82%, while decreasing it increased this distance by 47.16% (Fig. 4F, Table 1). Concurrently, the TNBC attractor basin size was inversely impacted by p65 degradation changes: a 2.5% decrease in p65 degradation increased the distance from the unstable to the TNBC state by 21.22%, while a 5.0% increase reduced this distance by 53.35%.

The above-described effects on the size of the attractor basin suggest explanations for the effect of varying p65 degradation as reported by Ren et al. (*26*). Specifically, the reduction in p65 degradation shrinks the HER2$^+$ attractor basin, facilitating the transition to the state of higher p65 levels, increasing cell proliferation and contributing to tumor progression. Conversely, the model predicts that increased p65 degradation would expand this basin, reducing the likelihood of this transition and thereby decreasing cell proliferation.

	Wild-Type			p65 degradation 2.5% lower			p65 degradation 5% higher		
Specie (molecule number)	HER2	Unstable	TN	HER2	Unstable	TN	HER2	Unstable	TN
p50	32491.3	76472	150491	33968.8	68630.7	156382	30449.1	96943	133008
p65	115566	260132	535271	123303	239395	573457	103958	316153	444084
NFkB	5893.33	31221.9	126429	6573.79	25786.8	140751	4968.14	48103.6	92705.9
RNAp50	104.38	245.66	483.44	109.12	220.47	502.36	97.82	311.42	427.28
RNAp65	134.99	303.86	625.25	140.43	272.65	653.11	127.50	387.76	544.67
p50 variation (%)				4.55	-10.25	3.91	-6.29	26.77	-11.62
p65 variation (%)				6.69	-7.97	7.13	-10.04	21.54	-17.04
NFkB variation (%)				11.55	-17.41	11.33	-15.70	54.07	-26.67
RNAp50 variation (%)				4.55	-10.25	3.91	-6.29	26.77	-11.62
RNAp65 variation (%)				4.03	-10.27	4.46	-5.55	27.61	-12.89
HER2-to-instable distance	151108.01			121156.10			222369.42		
TN-to-instable distance	284921.54			345395.01			132917.36		
HER2-to-unstable distance variation (%)				-19.82			47.16		
TN-to-unstable distance variation (%)				21.22			-53.35		

Table 1. Effects of Mutation on the Size of Attractor Basins. Comparison between wild-type and mutant stationary states. The table shows the percentage variation in the stationary molecule numbers of NF-κB and its subunits p50 and p65 resulting from the indicated changes in the p65 degradation rate. It also indicates the variations in the distances from the HER2$^+$ and TNBC stationary states to the unstable states.

To verify whether the above-described effects on the basin sizes influence transition probabilities, we carried out 120 stochastic simulations of HER2+ cells with p65 degradation reduced by 2.5%. All cells moved to a higher p65 level basin within 30 days, aligning with Ren et al.'s (*26*) findings on enhanced cell proliferation, reinforcing that mutations reducing the size of an attractor basin increase the probability of a cell departing from this attractor. In contrast, another set of 120 simulations with a 5% increase in p65 degradation showed no transitions over 20 years. It indicates that mutations that increase the size of an attractor basin decrease the probability of a cell's departure from this attractor, , thereby reducing cell proliferation, in agreement with Ren et al. (*26*). Taken together, these findings highlight the potential of p65 as a target for Targeted Protein Degradation, an emerging concept in drug discovery (*27*).

Conclusions

We propose a model that is sufficiently small to allow for a detailed analysis based on dynamic systems theory, yet large enough to encompass the key biological mechanisms behind the gene expression levels it intends to describe. Additionally, we performed the model calibration in two independent steps. First, we calibrated the model against cell data at the stationary states, followed by a time-dependent calibration to reproduce the dynamics of the gene expression recovery levels. Interestingly, the model could not reproduce the dynamic behavior with the same accuracy as it did for the static states, indicating that the effect of additional regulators was missing. This outcome suggests that our model was not constructed with an unnecessary number of parameters, which could have resulted in overfitting.

Remarkably, such a small model could offer explanations not only for the *in vitro* data it was calibrated against but also for other *in vitro* experiments (*26*) and patient-derived data (*5*, *6*, *23*). This includes explaining the p65-p50 RNA correlation in $HER2^+$ and TNBC, in both bulk and single-cell data. In fact, our modeling strategy mirrors the approach of a biologist who selects specific mechanisms to replicate in an *in vitro* assay, aiming to understand the broader *in vivo*, systemic behavior.

By showing how stochasticity at the molecular level leads to heterogeneity in cells and tissues, our work provides an explanation for recent findings about BC heterogeneity (*5*, *6*). This result can potentially impact clinical research by contributing to BC classification, which plays a critical role in determining patient-specific treatment. This can also contribute to personalized medicine.

By simulating variations in NF-κB dimer availability, our model serves as a platform for preliminary drug testing, particularly for strategies based on Targeted Protein Degradation. Additionally, the current version of the model is ready for diverse expansions. For instance, including target genes such as TWIST, SIP1, and SLUG can enhance our understanding of their roles in EMT, contributing to BC metastasis.

The finding that stochastic fluctuations can induce cell-subtype transitions is particularly interesting. It not only proposes an explanation for tumor heterogeneity but also supports the epigenetic attractor landscape model proposed by Waddington and Kauffman, specifically the association between attractor basins and cellular subtypes. Moreover, our model introduces two enhancements to these well-established general models. First, the model proposes that the key factor influencing how mutations affect transition probability lies in the size of the attractor basins. This offers a valuable tool for understanding and predicting the conditions necessary to trigger or prevent these transitions, because the size of the basins can be estimated from the relative distance between the stable states. Second, the model provides a detailed description of how eigenvectors contribute to transitions between basins of attraction. It proposes a specific pathway for transitions between the subtypes of these basins and offers an explanation for their irreversible nature. This irreversibility arises from two key factors: the relative weakness of the eigenvectors positioned between the stable states and the distance between these states. The weakness of the eigenvectors allows fluctuations to override their directionality, while the

distance between the states affects the likelihood of a fluctuation being strong enough to push the system across the unstable position and into another attractor basin.

Finally, this work stresses the advantages of an open-box model building strategy. In this approach, relatively small models, well described by dynamic system theory, successfully reproduce specific cellular processes. Consequently, these small models can be interconnected to build larger models that capture the complex interplay between different cellular processes. Successful examples of this strategy can already be seen in the literature (*28–31*), including its combination to well-succeeded black-box strategies (*32*).

MATERIALS AND METHODS

Cell culture and Real-Time Reverse Transcription Polymerase Chain Reaction (RT-qPCR)

The human BC cell lines MDA-MB-231 and HCC-1954 were cultured as previously described (*17*). Total RNA was isolated using TRIzol reagent (Thermo Fisher) according to the manufacturer's instructions. Then, 2 µg of RNA were treated with the DNase Amplification Grade I Kit (Thermo Fisher) and reverse transcribed into cDNA using the Superscript-II kit (Thermo Fisher) following the manufacturer's protocol. RT-qPCR was performed with SYBR Green Master Mix (Bio-Rad) in a Rotor-Gene Q (Qiagen) under previously reported conditions (*17*). Each sample was examined in triplicate. ACTB and GAPDH were used as reference genes for the mRNA levels. Fold expression was calculated according to the ΔΔCt method (*33*).

Building the Gene Regulatory Network

In our model, gene activation is described by a set of three-step reactions (*34*): a reversible reaction where the transcription factor (TF) binds to the gene's regulatory region, followed by two irreversible reactions for mRNA and protein synthesis (Fig. 1D and S1). This strategy is consistently applied to describe the transcriptional activation of all five genes: p65, p50, TWIST1, SLUG, and SIP1. We applied the law of mass action to derive a set of ODEs that describe the model dynamics (Fig. S2). The RNA levels were estimated from our RT-qPCR data (Fig. 1C) and compared to the estimated number of RNA molecules in a mammalian cell (Table S1). To ensure model accuracy, we assumed that only two copies of each gene are present.

Bistability analysis and model calibration

To determine if our model exhibits bistability, we used the Chemical Reaction Network Toolbox (34), which provides a set of kinetic constants that guarantee bistability along with the corresponding steady states. We then calibrated the full model by fixing the kinetic parameters as determined in (*35*), (Table S1). We utilized COPASI (*36*), a software tool for simulating and analyzing biochemical networks, for both calibrations: for the stationary states (Fig. 2A) and for recovery time after treatment with the NF-κB inhibitor DHMEQ (Fig. 2B). To solve the model equations during the calibration, we used the following parameters in COPASI: Relative Tolerance $1e^{-6}$, Absolute Tolerance $1e^{-12}$, and Maximum Internal Steps $1e^{5}$. The method used was 'LSDODA'.

Model simulation and landscape surface

All deterministic and stochastic simulations were performed using COPASI (*36*). For the deterministic simulations, we employed the same methods and parameters as previously mentioned. For the stochastic simulations, we utilized tau-leaping, a variant of the Gillespie algorithm, setting epsilon (the interval during which multiple reactions can take place) to 1E-3 and setting the maximum internal steps to 100 million $1e^{8}$). To construct the epigenetic attractor landscape, we modified the MATLAB code from reference (*37*). In our adaptation, instead of randomly exploring different positions in the phase space, we divided it into one million ($1e^{6}$) small, equally-sized squares. Additionally, we replaced the ode45 solver with ode15s, which is specialized for Differential Algebraic Equations. This significantly accelerates the code.

Validating Spearman correlation

We validated the correlations from our simulations using a cohort of 34 basal and 17 $HER2^+$ untreated patients (*23*, *38*). To ensure comparability, we randomly selected 34 basal and 17 $HER2^+$ single-cell stochastic simulations from our set of 120. For each simulation, we randomly selected one pair of p50 and p65 RNA molecule numbers and calculated the correlation across the entire set of selected simulations. These pairs represent the RNA levels of different cells at various moments. Figures 3A and 3B illustrate the correlation from one such set of simulations. To construct the table in Figure 3C, we repeated this process 100 times, only including sets where the correlation p-value was less than $5.0e^{-3}$.

REFERENCES

1. C. H. Waddington, *The strategy of the genes* (Allen and Unwin, London, 1957).

2. S. Kauffman, Differentiation of malignant to benign cells. *J. Theor. Biol.* **31**, 429–451 (1971).

3. J. Wang, L. Xu, E. Wang, Potential landscape and flux framework of nonequilibrium networks: robustness, dissipation, and coherence of biochemical oscillations. *Proc Natl Acad Sci USA*. **105**, 12271–12276 (2008).

4. C. M. Perou, T. Sørlie, M. B. Eisen, M. van de Rijn, S. S. Jeffrey, C. A. Rees, J. R. Pollack, D. T. Ross, H. Johnsen, L. A. Akslen, O. Fluge, A. Pergamenschikov, C. Williams, S. X. Zhu, P. E. Lønning, A. L. Børresen-Dale, P. O. Brown, D. Botstein, Molecular portraits of human breast tumours. *Nature*. **406**, 747–752 (2000).

5. W. Chung, H. H. Eum, H.-O. Lee, K.-M. Lee, H.-B. Lee, K.-T. Kim, H. S. Ryu, S. Kim, J. E. Lee, Y. H. Park, Z. Kan, W. Han, W.-Y. Park, Single-cell RNA-seq enables comprehensive tumour and immune cell profiling in primary breast cancer. *Nat. Commun.* **8**, 15081 (2017).

6. S. Z. Wu, G. Al-Eryani, D. L. Roden, S. Junankar, K. Harvey, A. Andersson, A. Thennavan, C. Wang, J. R. Torpy, N. Bartonicek, T. Wang, L. Larsson, D. Kaczorowski, N. I. Weisenfeld, C. R. Uytingco, J. G. Chew, Z. W. Bent, C.-L. Chan, V. Gnanasambandapillai, C.-A. Dutertre, L. Gluch, M. N. Hui, J. Beith, A. Parker, E. Robbins, D. Segara, C. Cooper, C. Mak, B. Chan, S. Warrier, F. Ginhoux, E. Millar, J. E. Powell, S. R. Williams, X. S. Liu, S. O'Toole, E. Lim, J. Lundeberg, C. M. Perou, A. Swarbrick, A single-cell and spatially resolved atlas of human breast cancers. *Nat. Genet.* **53**, 1334–1347 (2021).

7. F. Christian, E. L. Smith, R. J. Carmody, The Regulation of NF-κB Subunits by Phosphorylation. *Cells*. **5** (2016), doi:10.3390/cells5010012.

8. M. H. Park, J. T. Hong, Roles of NF-κB in Cancer and Inflammatory Diseases and Their Therapeutic Approaches. *Cells*. **5** (2016), doi:10.3390/cells5020015.

9. J. W. Gordon, J. A. Shaw, L. A. Kirshenbaum, Multiple facets of NF-κB in the heart: to be or not to NF-κB. *Circ. Res.* **108**, 1122–1132 (2011).

10. M. R. Zinatizadeh, B. Schock, G. M. Chalbatani, P. K. Zarandi, S. A. Jalali, S. R. Miri, The Nuclear Factor Kappa B (NF-kB) signaling in cancer development and immune diseases. *Genes Dis.* **8**, 287–297 (2021).

11. N. Khurana, S. C. Sikka, Targeting Crosstalk between Nrf-2, NF-κB and Androgen Receptor Signaling in Prostate Cancer. *Cancers (Basel)*. **10** (2018), doi:10.3390/cancers10100352.

12. F.-I. D. Dimitrakopoulos, A. E. Kottorou, M. Kalofonou, H. P. Kalofonos, The Fire Within: NF-κB Involvement in Non-Small Cell Lung Cancer. *Cancer Res.* **80**, 4025–4036 (2020).

13. Q. Li, G. Yang, M. Feng, S. Zheng, Z. Cao, J. Qiu, L. You, L. Zheng, Y. Hu, T. Zhang, Y. Zhao, NF-κB in pancreatic cancer: Its key role in chemoresistance. *Cancer Lett.* **421**, 127–134 (2018).

14. C. Kaltschmidt, C. Banz-Jansen, T. Benhidjeb, M. Beshay, C. Förster, J. Greiner, E. Hamelmann, N. Jorch, F. Mertzlufft, J. Pfitzenmaier, M. Simon, J. Schulte Am Esch, T. Vordemvenne, D. Wähnert, F. Weissinger, L. Wilkens, B. Kaltschmidt, A Role for NF-κB in Organ Specific Cancer and Cancer Stem Cells. *Cancers (Basel)*. **11** (2019), doi:10.3390/cancers11050655.

15. D. Verzella, A. Pescatore, D. Capece, D. Vecchiotti, M. V. Ursini, G. Franzoso, E. Alesse, F. Zazzeroni, Life, death, and autophagy in cancer: NF-κB turns up everywhere. *Cell Death Dis.* **11**, 210 (2020).

16. Y. Xia, S. Shen, I. M. Verma, NF-κB, an active player in human cancers. *Cancer Immunol. Res.* **2**, 823–830 (2014).

17. B. R. B. Pires, A. L. Mencalha, G. M. Ferreira, W. F. de Souza, J. A. Morgado-Díaz, A. M. Maia, S. Corrêa, E. S. F. W. Abdelhay, NF-kappaB Is Involved in the Regulation of EMT Genes in Breast Cancer Cells. *PLoS ONE*. **12**, e0169622 (2017).

18. M.-H. Sung, N. Li, Q. Lao, R. A. Gottschalk, G. L. Hager, I. D. C. Fraser, Switching of the relative dominance between feedback mechanisms in lipopolysaccharide-induced NF-κB signaling. *Sci. Signal.* **7**, ra6 (2014).

19. H. L. Pahl, Activators and target genes of Rel/NF-kappaB transcription factors. *Oncogene*. **18**, 6853–6866 (1999).

20. M. Feinberg, *Foundations of chemical reaction network theory* (Springer International Publishing, Cham, 2019), vol. 202 of *Applied Mathematical Sciences*.

21. H.-Y. Li, Zero eigenvalue analysis for the determination of multiple steady states in reaction networks. *Zeitschrift für Naturforschung A*. **53**, 171–177 (1998).

22. S. Huang, I. Ernberg, S. Kauffman, Cancer attractors: a systems view of tumors from a gene network dynamics and developmental perspective. *Semin. Cell Dev. Biol.* **20**, 869–876 (2009).

23. Z. Kan, Y. Ding, J. Kim, H. H. Jung, W. Chung, S. Lal, S. Cho, J. Fernandez-Banet, S. K. Lee, S. W. Kim, J. E. Lee, Y.-L. Choi, S. Deng, J.-Y. Kim, J. S. Ahn, Y. Sha, X. J. Mu, J.-Y. Nam, Y.-H. Im, S. Lee, W.-Y. Park, S. J. Nam, Y. H. Park, Multi-omics profiling of younger Asian breast cancers reveals distinctive molecular signatures. *Nat. Commun.* **9**, 1725 (2018).

24. Materials and Methods are available at the end of the document.

25. E. Cerami, J. Gao, U. Dogrusoz, B. E. Gross, S. O. Sumer, B. A. Aksoy, A. Jacobsen, C. J. Byrne, M. L. Heuer, E. Larsson, Y. Antipin, B. Reva, A. P. Goldberg, C. Sander, N. Schultz, The cBio cancer genomics portal: an open platform for exploring multidimensional cancer genomics data. *Cancer Discov.* **2**, 401–404 (2012).

26. C. Ren, X. Han, C. Lu, T. Yang, P. Qiao, Y. Sun, Z. Yu, Ubiquitination of NF-κB p65 by FBXW2 suppresses breast cancer stemness, tumorigenesis, and paclitaxel resistance. *Cell Death Differ.* **29**, 381–392 (2022).

27. J. M. Tsai, R. P. Nowak, B. L. Ebert, E. S. Fischer, Targeted protein degradation: from mechanisms to clinic. *Nat. Rev. Mol. Cell Biol.* (2024), doi:10.1038/s41580-024-00729-9.

28. A. Adelaja, B. Taylor, K. M. Sheu, Y. Liu, S. Luecke, A. Hoffmann, Six distinct NFκB signaling codons convey discrete information to distinguish stimuli and enable appropriate macrophage responses. *Immunity*. **54**, 916-930.e7 (2021).

29. Y. Arkun, M. Yasemi, Dynamics and control of the ERK signaling pathway: Sensitivity, bistability, and oscillations. *PLoS ONE*. **13**, e0195513 (2018).

30. M. Pan, P. J. Gawthrop, J. Cursons, E. J. Crampin, Modular assembly of dynamic models in systems biology. *PLoS Comput. Biol.* **17**, e1009513 (2021).

31. S. W. Michnick, E. D. Levy, The modular cell gets connected. *Science*. **375**, 1093–1094 (2022).

32. I. M. Chamseddine, K. A. Rejniak, Hybrid modeling frameworks of tumor development and treatment. *Wiley Interdiscip. Rev. Syst. Biol. Med.* **12**, e1461 (2020).

33. T. D. Schmittgen, K. J. Livak, Analyzing real-time PCR data by the comparative C(T) method. *Nat. Protoc.* **3**, 1101–1108 (2008).

34. F. J. P. Lopes, F. M. C. Vieira, D. M. Holloway, P. M. Bisch, A. V. Spirov, Spatial bistability generates hunchback expression sharpness in the Drosophila embryo. *PLoS Comput. Biol.* **4**, e1000184 (2008).

35. B. Schwanhäusser, D. Busse, N. Li, G. Dittmar, J. Schuchhardt, J. Wolf, W. Chen, M. Selbach, Global quantification of mammalian gene expression control. *Nature*. **473**, 337–342 (2011).

36. S. Hoops, S. Sahle, R. Gauges, C. Lee, J. Pahle, N. Simus, M. Singhal, L. Xu, P. Mendes, U. Kummer, COPASI--a COmplex PAthway SImulator. *Bioinformatics*. **22**, 3067–3074 (2006).

37. X. Zhang, K. H. Chong, L. Zhu, J. Zheng, A Monte Carlo method for in silico modeling and visualization of Waddington's epigenetic landscape with intermediate details. *BioSystems*. **198**, 104275 (2020).

38. Whole-exome sequencing of 187 primary tumors from a Korean breast cancer cohort (SMC). (2018), (available at https://www.cbioportal.org/study/summary?id=brca_smc_2018).

Acknowledgments: We thank Alexander Hoffmann and Mary Sehl for their inspiring discussions about the paper's results and perspectives, and Mariana C. Lopes for her assistance with figure design.

Funding:

Brazilian Council for Scientific and Technological Development (CNPq) grants: 200176/2022-6 (FL), 420264/2018-3 (EA, RB). Carlos Chagas Filho Foundation for Research Support of the State of Rio de Janeiro (FAPERJ) grant E-26/010.101086/2018 (EA, RB).

Author contributions:

Conceptualization: EA

Methodology: FL, BRBP, AABL, RB, EA

Investigation: FL, BRBP, AABL, RB, EA

Visualization: FL, AABL

Funding acquisition: EA

Project administration: EA

Supervision: EA

Writing – original draft: FL

Writing – review & editing: FL, BRBP, EA

Competing interests: Authors declare that they have no competing interests.

Data and materials availability: All data are available in the main text or the supplementary materials.